Electronic dispersions of a stable twisted bilayer phosphorene in 2O-tαP phase

Douxing Pan

View Online   Export Citation   CrossMark

ARTICLES YOU MAY BE INTERESTED IN

Publisher's Note: "Electronic dispersions of a stable twisted bilayer phosphorene in 2O-tαP phase" [J. Appl. Phys. 129, 055101 (2021)]
Journal of Applied Physics **129**, 119901 (2021); https://doi.org/10.1063/5.0046681

Probing the phonon mean free paths in dislocation core by molecular dynamics simulation
Journal of Applied Physics **129**, 055103 (2021); https://doi.org/10.1063/5.0038265

Twisted monolayer black phosphorus nanoribbbons: Tunable electronic and optical properties
Journal of Applied Physics **127**, 094303 (2020); https://doi.org/10.1063/1.5138704

Electronic dispersions of a stable twisted bilayer phosphorene in 2O-tαP phase

View Online   Export Citation   CrossMark

Douxing Pan[1,2,3,4,a] (iD)

AFFILIATIONS

[1]School of Mathematics and Physics, University of Science and Technology Beijing, Beijing 100083, People's Republic of China
[2]Beijing Institute of Nanoenergy and Nanosystems, Chinese Academy of Sciences, Beijing 101400, People's Republic of China
[3]School of Nanoscience and Technology, University of Chinese Academy of Sciences, Beijing 100049, People's Republic of China
[4]State Key Laboratory of Nonlinear Mechanics, Institute of Mechanics, Chinese Academy of Sciences, Beijing 100190, People's Republic of China

[a]Author to whom correspondence should be addressed: pandx@lnm.imech.ac.cn

ABSTRACT

It is reported for the electronic properties of an in-plane twisted bilayer phosphorene, known as the 2O-tαP phase, and the only dynamically stable phase beyond the AB stacking. This was achieved using first-principles calculations, a generalized empirical tight-binding model inclusive of electric field effects, and a two-parameter low energy effective model, the latter two providing an efficient scheme for nanoelectronics related applications. The tight-binding model reproduces a global fit to the first-principles dispersion, and the low energy model provides more accurate near-gap bands. Both are orders-of-magnitude faster and less memory-intensive than performing first-principles calculations. The twisted 2O-tαP structure possesses a direct bandgap of 1.27 eV, larger than that of the shifted AB structure (1.03 eV). The hole and electron polar effective mass anisotropy ratios are 27.34 and 1.95, respectively. An important observation is that the layer twisting results in the removal of Dirac cones as a reflection of a different band topology compared to the AB one, while the twofold degeneracy at the Brillouin zone boundary and the symmetry of the energy surface are both broken by an external vertical electric field. With an increasing electric field strength, a decreasing bandgap and an increasing energy difference between the valence band maximum and the twisted band point are both predicted by the tight-binding model and the low energy model.

Published under license by AIP Publishing. https://doi.org/10.1063/5.0039736

INTRODUCTION

Companied with the successful realization of graphene (i.e., a single layer of graphite),[1,2] two-dimensional (2D) layered materials such as silicene (monolayer silicon)[3] and transition metal dichalcogenides (TMDCs) such as monolayer molybdenum disulfide (MoS_2), have drawn significant attention due to their potential application in the next generation of nanoelectronic and optoelectronic devices.[3–5] However, graphene is a semi-metal with no bandgap, severely limiting its applications in nanotransistors and functional devices.[4] Several experiments have indicated that the mobility values of monolayer MoS_2 might be overestimated due to the capacitive coupling between the gates of the devices.[5,6] Recent exfoliation of orthorhombic black phosphorus (BP) has attracted interest in phosphorus-based 2D materials due to their large bandgaps and high charge carrier mobilities as well as the widely tunable

absorption of the resulting few layered compounds.[7–9] The double-atomically thin BP layer, so-called phosphorene, has interesting and unique mechanical behaviors such as anisotropic elasticity and negative Poisson effect.[10–12] The individual phosphorene layers can be coupled by van der Waals (vdW) interaction forming bi/tri/few-layer phases up to the bulk material.[7,8] The resulting stacks can be characterized into three types: in-plane shifted, in-plane twisted, and a hybrid of the former two. Theoretically, numerous bilayer stackings are possible, including commensurate and incommensurate orderings; potential commensurate stackings have been studied within the framework of density functional theory (DFT).[14–18] Only two kinds of dynamically stable bilayer phosphorene phases have been discovered so far: the shifted AB stacking and the twisted 2O-tαP stacking. The former is the basic BP building unit and exists in nature. The latter is another candidate with an in-plane twist angle of ~70.5°. The 2O-tαP phase has been discovered by several

different methods[19,20] and recently fabricated experimentally in its multilayer form.[21] The 2O-tαP phase is the thermodynamic quasi-stable with relatively low formation energy and rather high inter-layer friction, comparable to the existing AB phase. In the low frequency region of the 2O-tαP Raman spectrum, the layer-breathing mode L-A[1] and the out-of-plane twisted mode L-A[2] were both revealed, and a recognizable cross stripe STM image was also simulated, but its electronic properties have not been studied yet.

In this work, we report, by first-principles calculations and two extended atomic orbital models, the electronic properties of the 2O-tαP stacking for the first time. Although DFT is a powerful tool for predicting the electronic properties of materials, it is often hard to see the physics and computationally inefficient for device simulations. Therefore, we propose a four-parameter, multiband empirical tight-binding (ETB) model, including an external electric field term, which could provide an overall full-zone agreement with the DFT calculations over a broad energy window. In order to more accurately model the near-gap band structure around the gamma (Γ) point, a low energy effective (LEE) model is extracted. The bandgap, the effective masses, and the twist angle induced two proximal valence band edges, as well as the electric field-induced tuning are all systematically studied as they are needed for both optical and quantum transport modelings.

DFT-BASED CALCULATIONS

The first-principles calculations within the DFT framework were carried out using the Vienna *ab initio* simulation package (VASP).[22,23] A previously optimized geometrical structure of the 2O-tαP phase, accounting for vdW dispersion forces, was directly employed as the structural input.[20] Figures 1(a) and 1(b) present its Bravais lattice with two orthorhombic basis vectors, a_1 and a_2, and the corresponding reduced Brillouin zone (BZ) with a high symmetry path along X−Γ−X−Y−Γ−Y−S−Γ−S, where the bases b_1 and b_2 construct the reciprocal cell. The projector augmented wave method was used to describe the interactions between ion cores and valence electrons.[24,25] The kinetic energy cutoff for the plane wave basis was set at 400 eV, which guarantees the total energies being converged to within several meV. We used the hybrid exchange and correlation functional of Heyd, Scuseria, and Ernzerhof (HSE06).[26,27] The convergence criterion of 10^{-4} eV was set for electronic iterations to reduce the relative energy error to parts per ten thousand. Reciprocal space for the supercell of the twisted BP was meshed as $10 \times 14 \times 1$ using a Monkhorst–Pack scheme centered at the Γ point.[28] A vacuum spacing of at least 15 Å was introduced so that the spurious interaction between isolated bilayers can be neglected in the periodic boundary condition. The macroscopic static dielectric tensor is calculated from linear response theory in the independent-particle approximation, including local field effects.[29,30] The 2O-tαP relative dielectric component ε_z along the out-of-plane direction is calculated as 1.543. Figure 2 shows the projected 2O-tαP band structures. One can see that half the contributions come from 3s orbitals [Fig. 2(a)], which mainly control the deep energy level down to the bottom valence band (BVB). All 3p states are located near the Fermi level [Figs. 2(b)–2(d)], mainly controlling the swallow energy level up to the top conduction band (TCB). The TCB is outputted to the thirty-sixth empty band to compare with the constructed ETB model for
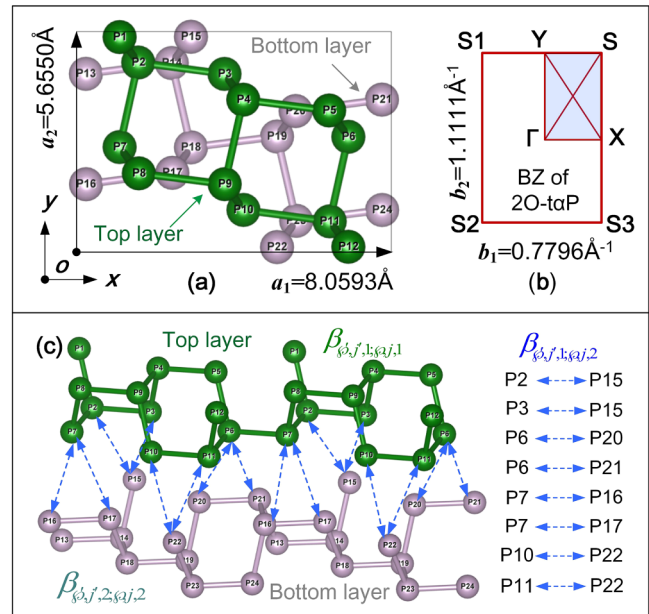

FIG. 1. Real/reciprocal unit cells and the corresponding hopping interactions of the in-plane twisted bilayer phosphorene. (a) 2O-tαP phase consists of 24 phosphorus atoms with a twisted angle of ∼70.5°, and a_1 and a_2 are the two basis vectors, constructing the unit cell. (b) Corresponding first BZ with b_1 and b_2 reciprocal bases, where the irreducible BZ is highlighted in blue. (c) Schematic representation of the intralayer hopping interactions in the top layer (green) and the bottom layer (gray), and the interlayer hopping interactions (blue dash). All symbols are defined in the main text. The optimized structural parameters were taken from Pan et al., J. Phys. Chem. Lett. 10(11), 3190–3196 (2019).

convenience. Thereinto, the $3p_y$ ingredient in Fig. 2(c) is relatively more important than the $3p_x$ ingredient in Fig. 2(b) assisting us to form a LEE model, especially the dispersion features along the path S−Γ−S. The $3p_z$ ingredient presented in Fig. 2(d) is closely related to the top valence band (TVB) together with the corresponding maximum value (VBM), and the bottom conduction band (BCB) together with its minimum point (CBM), playing a key role in describing the bandgap and the effective masses, as shall be discussed in the following.

FOUR-PARAMETER ETB MODEL

Figure 1(c) displays the intralayer and interlayer hopping interactions together with equivalences, assisting the construction of a Hamiltonian that describes the 2O-tαP band structure. The Hamiltonian is written in an ETB basis of Bloch sums on atomic orbitals,[31]

$$\Phi^{j,\ell}_{\wp k}(r) = \frac{1}{\sqrt{N}} \sum_n e^{i k \cdot (R_n + r_{j,\ell})} \phi_\wp(r - r_{j,\ell} - R_n), \quad (1)$$

where k is the reciprocal vector in a k-space, $\wp$ denotes the four angular momentum quantum numbers of the valence electrons
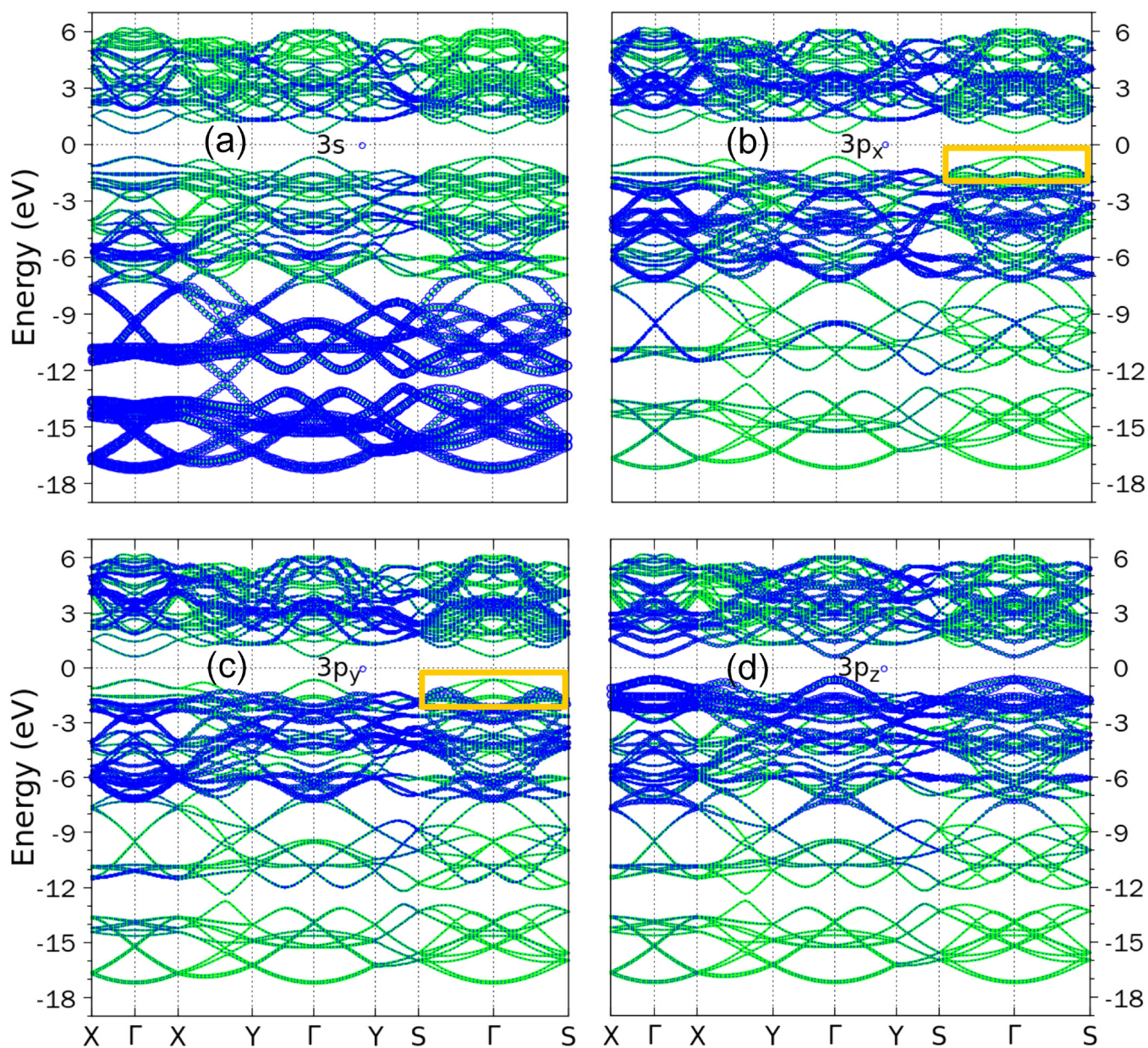
FIG. 2. Orbital projected band structures for the 2O-tαP stacking from the DFT calculations. Band curves are in green, and the Fermi level is set to zero. Blue circle sizes are proportional to the corresponding population in the states of (a) 3s, (b) $3p_x$, (c)$3p_y$, and (d)$3p_z$, respectively. The number of conduction bands is cut off to the 36 empty bands, while all the valence bands are included. The results obtained along the high symmetry path with X−Γ−(-X)−(-Y)−Γ−Y−(S1)−Γ−S are the same as that along X−Γ−X−Y−Γ−Y−S−Γ−S. The path S−Γ−S highlighted in yellow is within the ∼2 eV energy scope.

around each phosphorus atom, $\ell(=1,2)$ indicates the sequence number of two layers, and j (=1,2,...,Z_ℓ) is the sequence number of atoms in each layer (as shown in Fig. 1), R_n is the lattice vector of the nth unit cell relative to the lattice vector of the cell at the origin $R_0 = 0$ [Fig. 1(a)], $r_{j,\ell}$ is the atomic coordinate within a unit cell, $\phi_\wp$ are atomic-like orbitals (3s, $3p_x$, $3p_y$, and $3p_z$, see also Fig. 2),[32,33]

and N is the total number of unit cells in the periodic 2O-tαP lattice. A crystal electronic state is then given by

$$\psi_{bk}(r) = \sum_{\wp,j,\ell} C_{bk}^{\wp,j,\ell} \Phi_{\wp k}^{j,\ell}(r),$$ (2)

where b is the band index. The eigenenergy E_{bk}^{ETB} of the ETB wave function can be evaluated by substituting ψ_{bk} into the time-independent Schrödinger equation

$$H_{\text{EF}}^{\text{ETB}}\psi_{bk}(\mathbf{r}) = E_{bk}^{\text{ETB}}\psi_{bk}(\mathbf{r}), \tag{3a}$$

with

$$H_{\text{EF}}^{\text{ETB}} = -\frac{\hbar^2}{2m_0}\nabla^2 + \sum_{|\mathbf{r}-\mathbf{r}_{j,\ell}|}^{cutoff} V_{eff}(|\mathbf{r}-\mathbf{r}_{j,\ell}|) + H^{\text{EF}}, \tag{3b}$$

where m_0 is the free-electron mass, and V_{eff} is an effective short-ranged spherical atomic potential with a core electronic shielding effect by using a cutoff criterion of 2.5 Å and 3.6 Å for the intralayer and interlayer bindings, respectively. H^{EF} contains the electric field. Multiply Eq. (3a) from the left by a Bloch sum and integrating over all space, one finds

$$c_b^{\wp,j,\ell}\alpha_{\wp,j,\ell}^{\text{EF},b} + \sum_{\wp',\ell',j'\neq j}\sum_{\Delta\mathbf{R}_{n'}^n\in\{\mathbf{R}_{1NN}\}} c_b^{\wp',j',\ell'}\beta_{\wp',j',\ell'}^{\wp,j,\ell} e^{i\mathbf{k}\cdot(\Delta\mathbf{r}_{j',\ell'}^{j,\ell}+\Delta\mathbf{R}_{n'}^n)}$$
$$= \sum_{\wp',j',\ell'} c_b^{\wp',j',\ell'} E_{bk}^{\text{ETB}}\delta_{\wp',j',\ell'}^{\wp,j,\ell}, \tag{4}$$

with

$$\alpha_{\wp,j,\ell}^{\text{EF},b} = \int \phi_\wp^*(\mathbf{r}-\mathbf{r}_{j,\ell})H_{\text{EF}}^{\text{ETB}}\phi_\wp(\mathbf{r}-\mathbf{r}_{j,\ell})d\mathbf{r}, \tag{4a}$$

$$\beta_{\wp',j',\ell'}^{\wp,j,\ell} = \int \phi_\wp^*(\mathbf{r}-\mathbf{r}_{j,\ell})H_{\text{EF}}^{\text{ETB}}\phi_{\wp'}(\mathbf{r}-\mathbf{r}_{j',\ell'})d\mathbf{r}, \tag{4b}$$

$$\delta_{\wp',j',\ell'}^{\wp,j,\ell} = \int \phi_\wp^*(\mathbf{r}-\mathbf{r}_{j,\ell})\phi_{\wp'}(\mathbf{r}-\mathbf{r}_{j',\ell'})d\mathbf{r}, \tag{4c}$$

$$\Delta\mathbf{r}_{j',\ell'}^{j,\ell} = \mathbf{r}_{j',l'} - \mathbf{r}_{j,l} \text{ and } \Delta\mathbf{R}_{n'}^n = \mathbf{R}_{n'} - \mathbf{R}_n, \tag{4d}$$

where $c_b^{\wp,j,\ell} = C_{bk}^{\wp,j,\ell}e^{-i\mathbf{k}\mathbf{r}_{j,\ell}}$ (satisfying Einstein summation convention), and $\mathbf{R}_{1NN}$ indicates the 1st nearest-neighbor lattice vector. The first term on the left side of Eq. (4) is called on-site contribution considering a single spherical atom in isolation, with a constraint integral of Eq. (4a). In order to simplify the diagonalization, we reduce this term to a simpler form

$$\alpha_{\wp,j,\ell}^{\text{EF},b} = \alpha_\chi^b + ef + U^{\text{ETB}}\cdot\text{sign}(\ell), \quad (\chi:3s \text{ or } 3p), \tag{5a}$$

with

$$\text{sign}(\ell) = \begin{cases} +1 & \text{if } \ell = 1, \\ -1 & \text{if } \ell = 2, \end{cases} \tag{5b}$$

where α_χ^b is a known secondary level energy in the subshell of the valence electrons, and for the case of the phosphorus atom considered, are the $3s$ and $3p$ subshells with $\alpha_{3s}^b = -17.10$ eV, and

$\alpha_{3p}^b = -8.33$ eV, respectively,[34,35] which are reasonable according to Fig. 2. The parameter ef is a self-adjusted Fermi level related to electron filling and only leads to a constant shift in the band structure for an individual 2D material. For the 2O-tαP crystal considered, it becomes 6.961 eV and will be set as a reference of the remaining ETB band energies. U^{ETB} is a ETB electric potential energy difference controlled by the external electric field intensity E_T using $U^{\text{ETB}} = e_0 h_0 E_T/\varepsilon_z$, e_0 is the unit charge per free-electron, and $h_0 = 1$ Å is a unit distance between two polar plates.

The second term on the left side of Eq. (4) is usually called two-center electron hopping contribution, and Eq. (4b) is a transfer integral and defined as hopping parameters. On the right-hand side of Eq. (4), typically only the largest overlap term is included. Therefore, a non-trivial solution of Eq. (4) requires

$$\text{diag}\{E_{bk}^{\text{ETB}}\}|_{b=1}^{b=8Z_\ell} = \{\psi_{bk}\}^{-1}|_{b=1}^{b=8Z_\ell}[H_\beta^{\text{ETB}} + \text{diag}\{\alpha_{\wp,j,\ell}^{\text{EF},b}\}|_{b=1}^{b=8Z_\ell}]\{\psi_{bk}\}|_{b=1}^{b=8Z_\ell}, \tag{6}$$

and the effective Hamiltonian H_β^{ETB} can be decomposed into four block sub-matrices as

$$H_\beta^{\text{ETB}}(\mathbf{k}) = \begin{bmatrix} H_{\text{top-layer}}(\mathbf{k}) & H_{\text{top-bottom}}(\mathbf{k}) \\ H_{\text{top-bottom}}^\dagger(\mathbf{k}) & H_{\text{bottom-layer}}(\mathbf{k}) \end{bmatrix}_{8Z_\ell\times 8Z_\ell}, \tag{7}$$

where

$$H_{\text{top-layer}}(\mathbf{k}) = \left[\beta_{\wp',j',1}^{\wp,j,1}\sum_{\Delta\mathbf{R}_{n'}^n\in\{\mathbf{R}_{1NN}\}}e^{i\mathbf{k}\cdot(\Delta\mathbf{r}_{j',1}^{j,1}+\Delta\mathbf{R}_{n'}^n)}\right]_{4Z_1\times 4Z_1} \tag{7a}$$

and

$$H_{\text{bottom-layer}}(\mathbf{k}) = \left[\beta_{\wp',j',2}^{\wp,j,2}\sum_{\Delta\mathbf{R}_{n'}^n\in\{\mathbf{R}_{1NN}\}}e^{i\mathbf{k}\cdot(\Delta\mathbf{r}_{j',2}^{j,2}+\Delta\mathbf{R}_{n'}^n)}\right]_{4Z_2\times 4Z_2} \tag{7b}$$

are intralayer blocks closely related to the binding forces between two independent single phosphorene layers to form an individual integrated bilayer stacking, while

$$H_{\text{top-bottom}}(\mathbf{k}) = \left[\beta_{\wp',j',1}^{\wp,j,2}\sum_{\Delta\mathbf{R}_{n'}^n\in\{\mathbf{R}_{1NN}\}}e^{i\mathbf{k}\cdot(\Delta\mathbf{r}_{j',1}^{j,2}+\Delta\mathbf{R}_{n'}^n)}\right]_{4Z_1\times 4Z_2} \tag{7c}$$

contains the interlayer interactions, and note that

$$H_{\text{bottom-top}}(\mathbf{k}) = H_{\text{top-bottom}}^\dagger(\mathbf{k}) \text{ but } H_{\text{top-layer}}(\mathbf{k})$$
$$\neq H_{\text{bottom-layer}}(\mathbf{k}) \tag{8}$$

according to Fig. 1(c). The first sub-equation in Eq. (8) is due to the interlayer interactions actually satisfying the commutation relation. However, the second relation in Eq. (8) is rooted in an in-plane rotation operator between two layers leading to the local symmetry breaking, which is different from the AB stacking.[19,36]

For the hopping parameters in Eq. (7) between the jth and j'th sites, we can employ the formulas

$$\beta^{\wp,j,\ell}_{\wp',j',\ell'} = \begin{cases} \varpi_{\wp\wp'\sigma}, & (\wp, \wp':3s), \\ n_\mu \varpi_{\wp\wp'\sigma}, & (\wp:3s; \wp':3p_x, 3p_y, 3p_z), \\ (\delta_{\mu\mu'} - n_\mu n_{\mu'})\varpi_{\wp\wp'\pi} + n_\mu n_{\mu'}\varpi_{\wp\wp'\sigma}, & (\wp, \wp':3p_x, 3p_y, 3p_z), \end{cases} \quad (9)$$

where the direction cosines n_μ are expanded in terms of the unit basis of $\boldsymbol{e}_\mu$ as

$$n_\mu = \frac{(\Delta \boldsymbol{r}^{j,\ell}_{j',\ell'} + \Delta \boldsymbol{R}^n_{n'}) \cdot \boldsymbol{e}_\mu}{|\Delta \boldsymbol{r}^{j,\ell}_{j',\ell'} + \Delta \boldsymbol{R}^n_{n'}|}, \ (\mu, \mu' = x, y, z), \quad (9a)$$

and

$$\varpi_{\wp\wp'\Im} = \eta_{\wp\wp'\Im} \hbar^2/(m_0 |\Delta \boldsymbol{r}^{j,\ell}_{j',\ell'} + \Delta \boldsymbol{R}^n_{n'}|^2), \ (\Im:\sigma \ or \ \pi) \quad (9b)$$

is a popular scaling rule,[37,38] together with the 2O-tαP structure, affecting the width of the ETB energy bands. σ and π are the orbitals resolved along and perpendicular to the axis connecting two atoms, respectively, being labeled by a common magnetic quantum number $\Im$.

Utilizing Eqs. (5) and (9), as well as the following relationships

$$\beta^{3p_\mu,j,\ell}_{3s,j,\ell} = -\beta^{3s,j,\ell}_{3p_\mu,j,\ell} \ and \ \beta^{3p_{\mu'},j,\ell}_{3p_\mu,j,\ell} = \beta^{3p_\mu,j,\ell}_{3p_{\mu'},j,\ell} \quad (10)$$

between different hopping parameters and diagonalizing the matrix in Eq. (7), we can obtain a set of pre-eigenvalues by means of Eq. (6) for the 2O-tαP stacking. By fitting to the DFT energy band curves near the typical high symmetric points (here just for TVB, BVB in the Γ-point neighborhood, and TCB in the S-point neighborhood, respectively),[3,6,38] we find appropriate values to the ETB parameters $\eta_{\wp\wp'\Im}$ listed in Table I. The corresponding electronic properties from the ETB model are shown in Figs. 3–5, and Table II, respectively. The proposed model can be applied to AB stacked phosphorene, when we modify the second sub-relationship in Eq. (8) from the inequality to an equality. The earliest work had been done by Takao et al. for describing the band structure bulk/monolayer BP,[34] where the overlap integrals were calculated using Slater orbitals with Clementi's exponents.[39]

TABLE I. Parametric symbols and values (eV) in the global ETB model and local LEE model for the 2O-tαP stacking.

Models	Parameters			
	$\eta_{3s,3s,\sigma}$	$\eta_{3s,\wp,\sigma}$	$\eta_{\wp\wp'\sigma}$	$\eta_{\wp\wp'\pi}$
All-band ETB	−1.220	±1.841	2.840	−0.927
Local-band LEE	…	…	2.840	−0.741

ELECTRONIC STRUCTURE OF 2O-tαP STACKING

It can be seen from Fig. 3(a) that the ETB model reproduces the broad features of the DFT calculations. The ETB model shows that 96 band curves of the 2O-tαP stacking are divided into 24 sets with each set consisting of two pairs of bands. One can see from Fig. 3(b) that the lowest 12 pairs in the lower part of the energy window, 18 pairs below the Fermi level, and 18 pairs above the gap, can be roughly regarded as the 3s bands, the 3p bonding bands, and the 3p anti-bonding bands, respectively. They can be identified with the orbital projected electronic dispersion shown in Fig. 2. Each pair shows a twofold degeneracy at the zone boundary (e.g., Y−S line), but each set does not have fourfold degeneracy at the zone corner of the S point, as seen in Fig. 3(b), which is different from the AB stacking.[8,14,34,35] The difference originates from the local symmetry breaking of the twisted stacking order as verified by Eq. (8). In other words, for the 2O-tαP stacking, some neighboring sets are unable to connect with each other to form the conventional Dirac cones found in the AB stacking; this provides a practical way to open a gap in the band structure of an engineered BP stack. Figure 3(c) shows that the 2O-tαP stacking has a direct bandgap of 1.274 eV at the BZ center of the Γ-point, larger than that of the AB stacking (1.02 – 1.04 eV) within the HSE06 functional.[8,14,18] We found that the gap size always increases when $\eta_{\wp,\wp',\sigma}$ or $\eta_{\wp,\wp',\pi}$ increases, and the Hamiltonian elements related to $3p_z$ states are significantly affected by means of Eq. (7). This implies that the gap is governed by the $3p_z$ orbital coupling effect, and by means of Eq. (7c), indirectly affects the stability of the 2O-tαP stacking and the corresponding lattice constants.[19] It also illustrates the usefulness of a two-parameter tight-binding model as an effective model in the shallow energy zone for the 2O-tαP band structure theory and though limited for energies elsewhere in the 2O-tαP BZ.

Using the ETB model, we predicted the band structures in the perpendicular uniform electric field strengths of 0.15 V/Å and 0.35 V/Å for the 2O-tαP stacking, as shown in Figs. 4(a) and 4(b), respectively. Three main features are visible: (1) the twofold degeneracy at the BZ boundary is removed; (2) the bandgap is narrowed; and (3) the twisted band point (TBP) is lowered. The TBP is the band energy value located under the VBM, as labeled in Fig. 4(a), which is also identified by Cao et al. in the 90° twisted bilayer black phosphorus.[13] Without any rotation, the difference between TBP and VBM, or $E_{twist} = E_{VBM} − E_{TBP}$ as labeled in Fig. 4(b), is the largest; with the twist angle of 90°, the TBP is degenerate with the VBM. For the ~70.5° rotation, the TBP is close to VBM, between that of the former two stackings, and the difference is shown in the enlarged part of Fig. 3(c). Figure 4(c) shows the variation of the bandgap E_{gap} and the E_{twist} value as a function of the electric field strength: the bandgap presents a hybridization of a hyperbola-like curve and a close-to-linear dependence, just between the untwisted
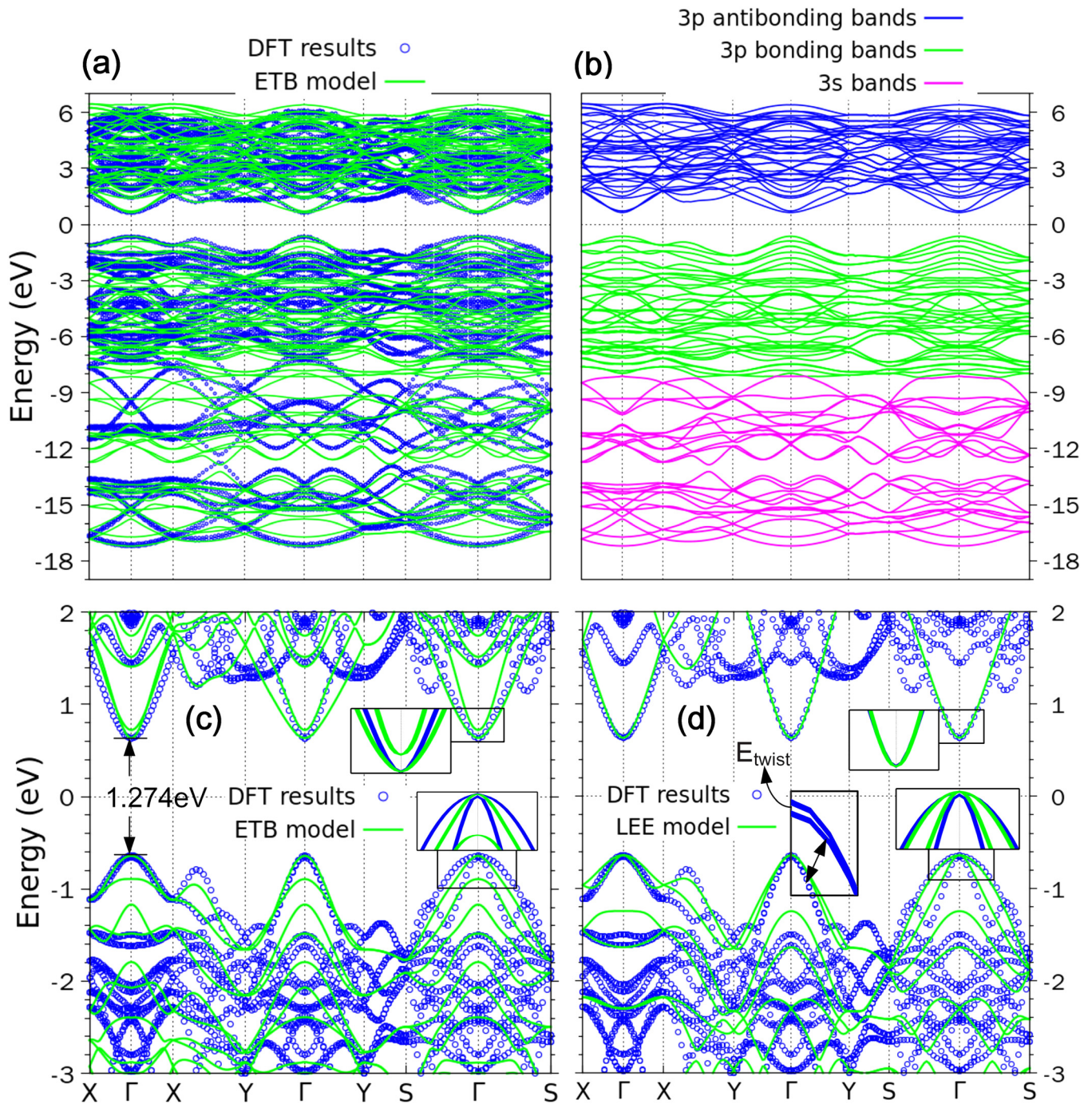
FIG. 3. Band structures of the 2O-tαP stacking from three different methods. (a) Comparison between DFT calculations (blue circles) and ETB model (green lines) over a wide energy range. (b) ETB bands are grouped into the mostly 3s bands (magenta lines), mostly 3p bonding bands (green lines), and mostly 3p anti-bonding bands (blue lines), respectively. (c) Comparison between DFT calculations (blue circles) and ETB model (green lines) in describing band structures in the local window near the Fermi level. (d) Comparison between DFT calculations (blue circles) and LEE model (green lines) in describing band structures in the local window near the Fermi level. The zoom-in insets in (c) and (d) are BCBs and TVBs along the path of S–Γ–S for the detailed comparisons among three different simulated/modeled methods. The results obtained along the high symmetry path with X–Γ–(-X)–(-Y) –Γ–Y–(S1)–Γ–S are the same as that along X–Γ–X–Y–Γ–Y–S–Γ–S. An expanded window to focus on the path of Γ–Y in (d) from DFT calculations to highlight the non-degeneracy DFT bands with the difference of the VBM and TBP at the Γ-point labeled as E_{twist}.
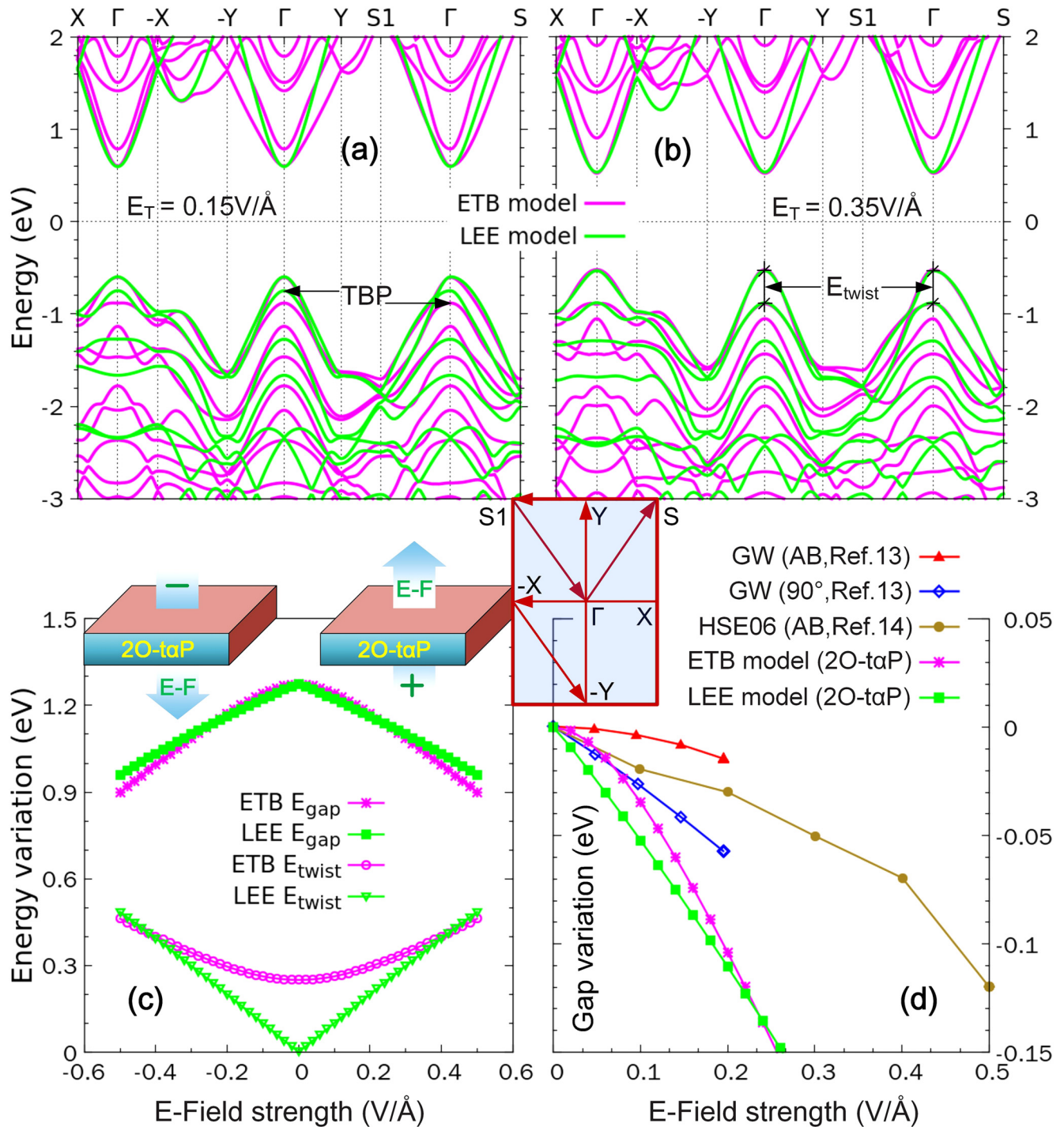
FIG. 4. ETB and LEE electronic structures of the 2O-tαP phase in a uniform electric field. Band structures in the uniform electric field of (a) 0.15 V/Å and (b) 0.35 V/Å predicted by the ETB model (magenta lines) and the LEE model (green lines), respectively. (c) Bandgap E_{gap} and the difference E_{twist} of the VBM and TBP as a function of the electric field strength predicted by the ETB model (in magenta) and the LEE model (in green), respectively, together with two schematic diagrams of the applied vertical electric field. (d) Variations of the bandgap with the electric field for different stacking orders from different calculations/modelings. The BZ path is along X$-\Gamma-$(-X)$-$(-Y)$-\Gamma-$Y$-$(S1)$-\Gamma-$S shown in the center light blue inset.
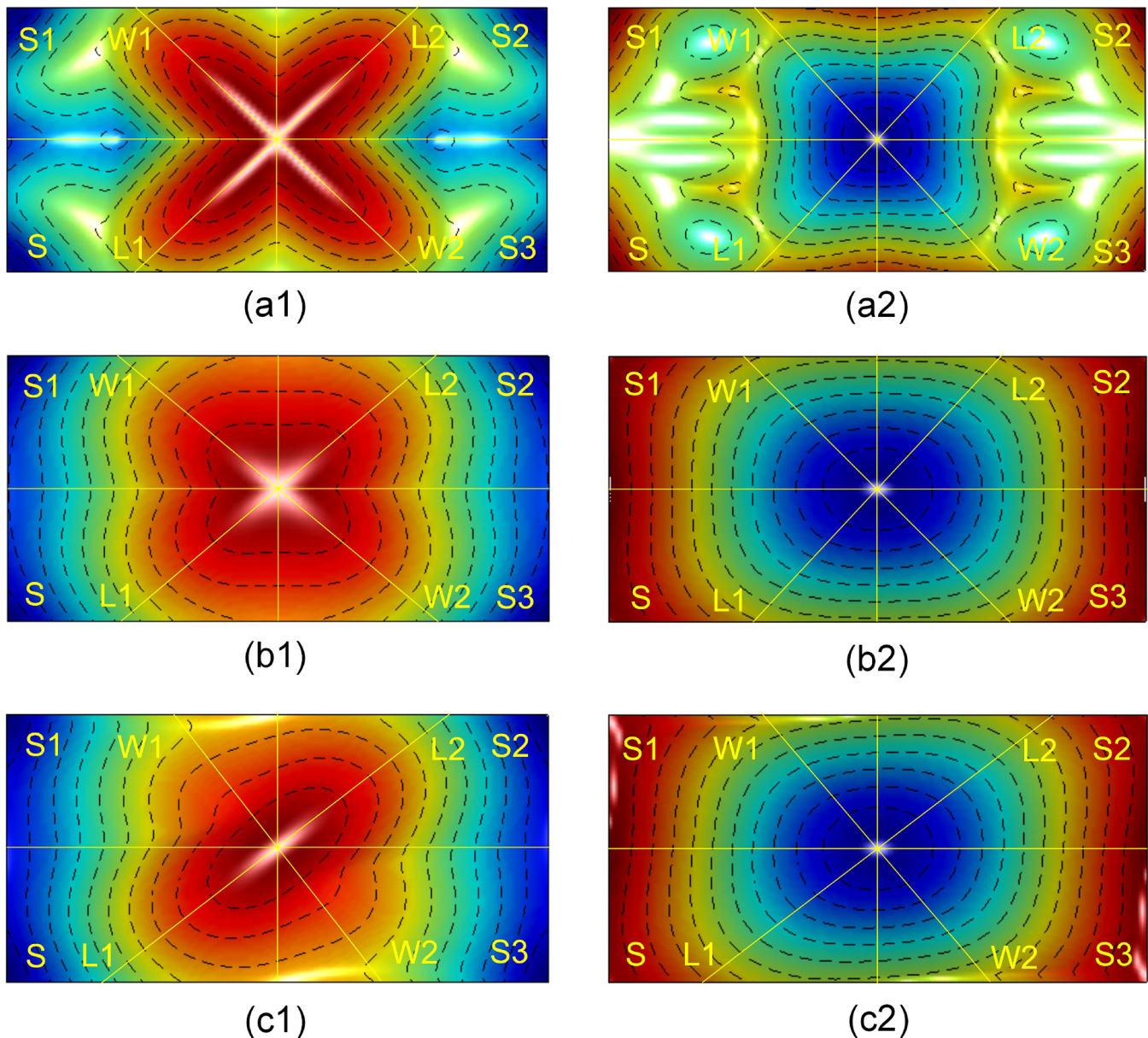
FIG. 5. 2D projected energy surface morphologies of the 2O-tαP phase in the full BZ. DFT calculated (a1) BCS and (a2) TVS. LEE modeled (b1) BCS and (b2) TVS. LEE predicted (c1) BCS and (c2) TVS subject to an electric field strength of 0.15 V/Å. The color indicates an increasing energy value from blue to red. L1–L2 and W1–W2, as well as the high symmetry paths all indicate the local extremal energy variation directions, and they are all highlighted in yellow. The hypsographic map is presented by a set of black dashed curves.

stacking and the 90° twisted stacking within the 0.07 V/Å field intensity, as shown in Fig. 4(d); E_{twist} presents a catenary-like trend, instead of linear. Unlike the linear dependence of the 90° twisted stacking due to its in-plane fourfold rotational symmetry, the even function behavior about the electric field intensity of the ∼70.5° E_{twist} comes from its twofold rotational symmetry.[20] Figure 4(d)

further shows the variations of the bandgap with the applied electric field for three typical stackings, which is a much more costly task for first-principles calculations, but the results from the ETB model can be compared with the results calculated by the HSE06 and GW methods.[13,14] As an example, the 51 points in Fig. 4(c) took roughly 150 s to compute using one core, whereas just one

TABLE II. Effective masses calculated from first-principles, references, as well as ETB and LEE models.

Conventional, effective mass	Hole (2O-tαP)			Electron (2O-tαP)		
	$m_x^*(m_0)$	$m_y^*(m_0)$	$m_{xy}^*(m_0)$	$m_x^*(m_0)$	$m_y^*(m_0)$	$m_{xy}^*(m_0)$
DFT/HSE06	0.753	0.268	1.147	0.311	0.191	0.239
ETB model	0.688	0.374	0.48	0.204	0.492	0.448
LEE model	1.045	0.408	0.955	0.293	0.264	0.303
From References	Hole (AB)		v_{hm}	Electron (AB)		v_{em}
DFT/PBE[8]	1.81	0.15	12.067	1.13	0.18	6.278
DFT/PBE[18]	2.7	0.11	24.545	1.32	0.11	12
DFT/PBE[43]	2.18	0.1	21.8	1.35	0.11	12.27
Polar, effective mass	Hole (2O-tαP)			Electron (2O-tαP)		
	$m_{h1}^*(m_0)$	$m_{h2}^*(m_0)$	v_{hm}	$m_{e1}^*(m_0)$	$m_{e2}^*(m_0)$	v_{em}
DFT/HSE06	7.312	0.268	27.336	0.371	0.191	1.946
ETB model	0.691	0.374	1.85	0.525	0.204	2.571
LEE model	1.354	0.408	3.321	0.335	0.264	1.272
Uniform electric field strength of 0.15 V/Å perpendicular to 2O-tαP						
ETB model	0.922	0.375	2.46	0.686	0.22	3.123
LEE model	1.296	0.396	3.27	0.331	0.264	1.256

point took about 30 h using 24 cores and the DFT code. In the DFT-based first-principles calculations, the vertical electric field is treated by adding an artificial dipole sheet in the 2D crystal cell,[29,40] which is essentially equivalent to increasing the potential energy difference of the 2O-tαP phase along its out-of-plane direction, similar to Eq. (5). Recently, Li *et al.*[41] proposed a self-consistent TB model for the gated multilayer phosphorene, where the trend of the bandgap decreasing with increasing electric-field strength is very similar with the model here, and their theoretical results are qualitatively consistent with the experimental ones presented in Ref. 42 indicating the usability of our ETB model. Revisiting the results from Figs. 2 and 3, one can see that the band structures obtained along the high symmetry path with X−Γ−X −Y−Γ−Y−S−Γ−S are the same as that along X−Γ−(-X)−(-Y)−Γ −Y−(S1)−Γ−S from two different methods. In the presence of an electric field, the band curves are not symmetrical about the Γ-point any more along the path of (S1)−Γ−S, although they remain symmetric along X−Γ−(-X)−(-Y)−Γ−Y.

Conventional effective masses were next computed using

$$\frac{m_0}{m_{\mu\mu'}^*} = \frac{m_0}{\hbar^2}\frac{\partial E_b(k)}{\partial k_\mu \partial k_{\mu'}}\bigg|_{k=\Gamma}, \quad (b:\text{TVB or BCB}), \quad (11)$$

where the TVB and BCB curves in a small region near the Γ-point are fitted using parabolas along the high symmetry paths of X−Γ−X and Y−Γ−Y, respectively, for m_x^* and m_y^* and along S−Γ−S for m_{xy}^*. A forward–backward difference method was used to evaluate the differentiations. The corresponding values are listed in Table II. Comparing with the effective mass values from the literature studies for the AB stacking, respectively,[8,18,43] we found that the AB stacking effective mass m_x^* along the short zigzag direction is always

larger than m_y^* along its long armchair direction, though very different values have been reported. On the other hand, the 2O-tαP stacking effective masses along the short lattice direction or the long reciprocal basis vector can be smaller than that along their long lattice direction or the short reciprocal one. For both stackings, the hole effective masses are overall larger than the electron effective masses, in line with other 2D materials.[3–6] We also found that for the AB stacking, the hole effective masses can be larger than $2m_0$, and the electron effective masses can be larger than m_0; but for the 2O-tαP stacking, the hole effective masses are always less than $2m_0$, and the electron effective masses are always smaller than m_0 using three different computational methods. The agreement between the DFT calculations and the ETB predictions is relatively good for the hole masses but less so for the electron ones. This result is typical of the sp^3 basis ETB model that tend to produce valence bands with more accurate dispersions than for the conduction bands.[44]

To investigate the angle dependence, we calculated the effective masses in the polar coordinate system in taking the directional derivative of the energy along the radius in the $\boldsymbol{k}$ direction as follows:

$$\frac{m_0}{\boldsymbol{m}_k^*} = \frac{m_0}{\hbar^2}\frac{\partial E_b(k)}{\partial k^2}\boldsymbol{e}_k\bigg|_{k=\Gamma}, \quad (b:\text{TVS or BCS; } \boldsymbol{k}=k\boldsymbol{e}_k). \quad (12)$$

On the basis of Eq. (12), we further define two ratios by $v_{hm} = m_{h1}^*/m_{h2}^*$ and $v_{em} = m_{e1}^*/m_{e2}^*$ to quantify the anisotropic behavior of the polar hole and electron effective masses, respectively, where the extremal hole effective mass values in the polar coordinate system are obtained from

$$m_{h1}^* = \max(\|\boldsymbol{m}_k^*|_{\Gamma\in\text{TVS}}\|) \text{ and } m_{h2}^* = \min(\|\boldsymbol{m}_k^*|_{\Gamma\in\text{TVS}}\|) \quad (13a)$$

in the Γ-point neighborhood of the 2D projected top valence energy surface [TVS, see Figs. 5(a1)–5(c1), and note that the Γ-point and the center of the energy surface coincide here, so in this case, we can use the same point to express both of them], while the polar electron effective mass extremums are obtained from

$$m_{e1}^{*} = \max(\|\boldsymbol{m}_{k}^{*}|_{\Gamma\in\text{BCS}}\|) \text{ and } m_{e2}^{*} = \min(\|\boldsymbol{m}_{k}^{*}|_{\Gamma\in\text{BCS}}\|) \quad (13b)$$

in the Γ-point neighborhood of the 2D projected bottom conduction energy surface [BCS, see Figs. 5(a2)–5(c2)]. Due to the zigzag and armchair directions overlapping their extremal ones according to the results by Çakır *et al.*,[18] we directly define two ratios v_{hm} and v_{em} by m_{x}^{*}/m_{y}^{*} for the hole and electron anisotropic characteristic degrees of the shifted AB stacking, respectively. It can be seen from Table II that the global extremums can be close to each other between the first-principles calculations and the ETB model, except for the maximal polar hole effective mass. The hole anisotropy ratios are 27.336 and 24.545 for the 2O-tαP stacking and the AB stacking, respectively, thus both of them with significant anisotropy, while the electron anisotropy ratios of the 2O-tαP stacking are all around 2, much smaller than that of the AB stacking, indicating a nearly isotropic feature.

FURTHER DISCUSSION

While the ETB model was introduced to reproduce the broad features of the 2O-tαP band structure, there is also the need for an accurate modeling of the near-gap band structure. Unfortunately, the ETB model and DFT calculations have substantial disagreements in that energy window. The discrepancy is most obvious along the path of S–Γ–S within the energy range of $\sim$0.4 eV in the inset of Fig. 3(c), that the first principles method gives one band in the conduction zone and two proximal bands in the valence zone, whereas the ETB model gives two conduction bands and two valence bands with a larger E_{twist}. Since the focus is now on the bands near the Fermi level, we develop a low energy effective model, i.e., the LEE model, based on the original ETB model and by properly modifying Eqs. (5a) and (9) as follows, respectively, i.e.,

$$\alpha_{\chi j,\ell}^{\text{EF},b} = \alpha_{\chi}^{b} + ef + \text{U}^{\text{LEE}} \cdot \text{sign}(\ell), \, (\chi: 3s \text{ or } 3p_z), \quad (14a)$$

where $\text{U}^{\text{LEE}} = \text{U}^{\text{ETB}}$, and

$$\beta_{\wp',j',\ell}^{\wp,j,\ell} = (\delta_{\mu\mu'} - n_{\mu}n_{\mu'})\varpi_{\wp\wp'\pi} + n_{\mu}n_{\mu'}\varpi_{\wp\wp'\sigma}, \, (\wp,\wp': 3p_y, 3p_z). \quad (14b)$$

It can be seen from Fig. 2 that although the bands near the Fermi level are affected by the on-site energies from the $3s$ and $3p$ subshells, the dominant contributor to the effective Hamiltonian is the $3p_z$ orbital. Meanwhile, comparing the $3p_x$ orbital in Fig. 2(b) with the $3p_y$ orbital in Fig. 2(c), the latter is more useful in constructing the new model, especially for the direction S–Γ–S highlighted in yellow. Equation (14) leads to a reduced-order LEE Hamiltonian matrix from the ETB one,

$$H_{\text{EF}}^{\text{ETB}} \rightarrow H_{\text{EF}}^{\text{LEE}}: \, [H_{\beta}^{\text{ETB}} + \text{diag}\{\alpha_{\wp',j,\ell}^{\text{EF},b}\}]_{8Z_{\ell} \times 8Z_{\ell}}$$
$$\rightarrow [H_{\beta}^{\text{LEE}} + \text{diag}\{\alpha_{\chi j,\ell}^{\text{EF},b}\}]_{4Z_{\ell} \times 4Z_{\ell}}. \quad (15)$$

The parameters of the LEE model are still obtained from the first-principles calculations and listed in Table I. The results from the LEE model are presented in Figs. 3(d), 4, 5(b), and 5(c), as well as Table II, respectively. It is necessary to point out, for the conduction branch from the band results shown in Fig. 3(c), there is yet some space to improve the fitting quality of the ETB model, which can be, in principle, achieved by using the machine learning (ML) approach to optimize the free parameters involved in the model and to minimize the relative error between the DFT and ETB bands.[45] However, in practice, limited to the number of parameters, this method cannot give consideration to two or more things: the ETB model can still not move the second conduction band too far nor could we significantly reduce E_{twist} and hardly present its physics significance revealed by our LEE model. In the future, by introducing spin–orbit coupling parameters and using advanced ML techniques, we will further improve the quality of 2O-tαP ETB model, as done by Nakhaee *et al.* for BiTeCl.[45]

As seen in Fig. 3(d), although the bandgaps are all the same value given by three methods, E_{twist} are different: 16.7 meV for HSE06, 2.1 meV for LEE, but 250.3 meV for ETB. For the 90° stacking, however, E_{twist} is smaller than 0.1 meV.[13] Furthermore, the above discrepancy within the $\sim$0.4 eV energy scope is now resolved: the redundant conduction band disappears, and the faraway valence band now moves sufficiently close to the band edge, but they do not merge into each other. The original ETB model's poor description near the band edges originates from the interference with the deep $3s$ orbital, and the excessive coupling between $3s$ and $3p$ subshell orbitals, which can be attributed to the parameters $\eta_{3s,3s,\sigma}$ and $\eta_{3s,\wp,\sigma}$, respectively. Using the new LEE model, we predict the band structures in the perpendicular uniform electric field strengths of 0.15 V/Å and 0.35 V/Å and the corresponding tuning behaviors for the 2O-tαP E_{gap}, E_{twist}, and ΔE_{gap}, as shown in Fig. 4. It can be seen that both E_{gap} and E_{twist} have a close-to-linear field dependence, closer to that of the GW calculations. Figures 5(b1) and 5(b2) exhibit the qualitative features (e.g., the hypsographic map, the local extremal energy variation, and the symmetry) of the 2D LEE BCS and TVS in the full BZ, respectively, which are close to that of the DFT calculations shown in Figs. 5(a1) and 5(a2), respectively. One can see that: (1) for TVS, the local minimal energy gradients are along the $\sim$45° and $\sim$135° directions, respectively, and the global maximal energy gradient directions are both along the right-angle side [Γ–Y in Fig. 1(b)]; (2) for BCS, the local minimum energy gradients are along $\sim$30° and $\sim$150° directions, respectively, and the local maximum energy gradient directions are both along the high symmetry paths; (3) the new model substantially improves the description of the local dispersion in the Γ-point neighborhood, especially for the BCS local dispersion [Fig. 5(b2)], rather close to that from DFT calculations [Fig. 5(a2)]. Also, it can be seen from Table II that the LEE model can be in better agreement with the DFT results for effective masses. We further examined the 2D projected BCS and TVS in the full BZ under the perpendicular uniform electric field strengths of 0.15 V/Å as shown in Fig. 5(c). It can be seen that the electric field distorts the overall BCS appearance and the corresponding features, different from those in Figs. 5(a) and 5(b). Finally, we use the constructed model to predict the polar effective masses near the Γ-point neighborhood of the full BZ for the 2O-tαP phase in an electric field of

0.15 V/Å. We found that the polar electron effective mass predicted by the LEE model is almost independent of the electric field, while this is not the case for the polar hole effective mass. The global polar effective mass extremums and the corresponding anisotropy ratios from the two proposed models are all listed in the table for a uniform electric field strength of 0.15 V/Å perpendicular to 2O-tαP.

CONCLUSION

In conclusion, the electronic dispersions of the in-plane twisted 2O-tαP bilayer phosphorene were studied for the first time using first-principles calculations and two atomic orbital models: the ETB model and the LEE model. The ETB model provides overall agreement with DFT results in the full BZ, but it gives an inaccurate description of the local bands near the gap, whereas the LEE model works well in that regime. The ETB model lays the foundation of the modified LEE model. We focused on the local energy window nearby the Fermi level to obtain the bandgap (1.27 eV), the 2D projected energy surface morphology features (the hypsographic map, the local extremal energy variation, and the symmetry), and the polar effective mass anisotropy ratios (27.34 and 1.95 for the hole and the electron), as well as the electric field behavior (two different types of tuning behaviors, and the unsymmetrical TVS and BCS). The non-existence of Dirac cones in the band topology of the 2O-tαP phase compared to the AB stacking is a consequence of the in-plane twist angle; the twofold degeneracy at the BZ boundary is removed by an external uniform electric field in the vertical direction. The models are both significantly faster than the first-principles calculations. Our study closely combines first-principles calculations with the empirical orbital models for the stable twisted bilayer phosphorene under an electric field, not only providing a suitable tool for modeling nanotransistors and other semiconductor devices, but also paving the way to theoretically study incommensurate stackings within the context of the combination of an ETB model or a LEE model and the perturbation theory as well as advanced ML techniques.

ACKNOWLEDGMENTS

DATA AVAILABILITY

The data that support the findings of this study are available within the article.

REFERENCES

[1] K. S. Novoselov, A. K. Geim, S. V. Morozov, D. Jiang, Y. Zhang, S. V. Dubonos, I. V. Grigorieva, and A. A. Firsov, "Electric field effect in atomically thin carbon films," Science **306**(5696), 666–669 (2004).

[2] A. K. Geim, "Graphene: Status and prospects," Science **324**(5934), 1530–1534 (2009).

[3] G. G. Guzmán-Verri and L. C. Lew Yan Voon, "Electronic structure of silicon-based nanostructures," Phys. Rev. B **76**(7), 75131 (2007).

[4] A. C. Ferrari, F. Bonaccorso, V. Fal'ko, K. S. Novoselov, S. Roche, P. Bøggild, S. Borini, F. H. L. Koppens, V. Palermo, and N. Pugno, "Science and technology roadmap for graphene, related two-dimensional crystals, and hybrid systems," Nanoscale **7**(11), 4598–4810 (2015).

[5] K. H. Liu, L. M. Zhang, T. Cao, C. H. Jin, D. A. Qiu, Q. Zhou, A. Zettl, P. D. Yang, S. G. Louie, and F. Wang, "Evolution of interlayer coupling in twisted molybdenum disulfide bilayers," Nat. Commun. **5**(1), 4966 (2014).

[6] G.-B. Liu, W.-Y. Shan, Y. G. Yao, W. Yao, and D. Xiao, "Three-band tight-binding model for monolayers of group-VIB transition metal dichalcogenides," Phys. Rev. B **88**(8), 85433 (2013).

[7] L. K. Li, Y. J. Yu, G. J. Ye, Q. Q. Ge, X. D. Ou, H. Wu, D. L. Feng, X. H. Chen, and Y. B. Zhang, "Black phosphorus field-effect transistors," Nat. Nanotechnol. **9**(5), 372–377 (2014).

[8] J. S. Qiao, X. H. Kong, Z.-X. Hu, F. Yang, and W. Ji, "High-mobility transport anisotropy and linear dichroism in few-layer black phosphorus," Nat. Commun. **5**(1), 4475 (2014).

[9] M. Alidoust, K. Halterman, D. X. Pan, M. Willatzen, and J. Akola, "Strain-engineered widely tunable perfect absorption angle in black phosphorus from first principles," Phys. Rev. B **102**(11), 115307 (2020).

[10] E. Mohammad, K. Khaliji, S. M. Tabatabaei, M. Pourfath, and R. Asgari, "Modulation of electronic and mechanical properties of phosphorene through strain," Phys. Rev. B **91**(11), 115412 (2015).

[11] J.-W. Jiang and H. S. Park, "Negative Poisson's ratio in single-layer black phosphorus," Nat. Commun. **5**(1), 4727 (2014).

[12] Y. Ding, Y. L. Wang, L. Shi, Z. J. Xu, and J. Ni, "Anisotropic elastic behaviour and one-dimensional metal in phosphorene," Phys. Status Solidi RRL **8**(11), 939–942 (2014).

[13] T. Cao, Z. L. Li, D. Y. Qiu, and S. G. Louie, "Gate switchable transport and optical anisotropy in 90° twisted bilayer black phosphorus," Nano Lett. **16**(9), 5542–5546 (2016).

[14] J. Dai and X. C. Zeng, "Bilayer phosphorene: Effect of stacking order on bandgap and its potential applications in thin-film solar cells," J. Phys. Chem. Lett. **5**(7), 1289–1293 (2014).

[15] A. Mukhopadhyay, L. Banerjee, A. Sengupta, and H. Rahaman, "Effect of stacking order on device performance of bilayer black phosphorene-field-effect transistor," J. Appl. Phys. **118**(22), 224501 (2015).

[16] T. Zhang, J.-H. Lin, Y.-M. Yu, X.-R. Chen, and W.-M. Liu, "Stacked bilayer phosphorene: Strain-induced quantum spin Hall state and optical measurement," Sci. Rep. **5**(1), 13927 (2015).

[17] M. Alidoust, M. Willatzen, and A. P. Jauho, "Fraunhofer response and supercurrent spin switching in black phosphorus with strain and disorder," Phys. Rev. B **98**(18), 184505 (2018).

[18] D. Çakır, C. Sevik, and F. M. Peeters, "Significant effect of stacking on the electronic and optical properties of few-layer black phosphorus," Phys. Rev. B **92**(16), 165406 (2015).

[19] D. X. Pan, T.-C. Wang, W. D. Xiao, D. M. Hu, and Y. G. Yao, "Simulations of twisted bilayer orthorhombic black phosphorus," Phys. Rev. B **96**(4), 041411 (2017).

[20] D. X. Pan, C. S. Liu, G.-B. Liu, S. Feng, and Y. G. Yao, "Physical fingerprints of the 2O-tαP phase in phosphorene stacking," J. Phys. Chem. Lett. **10**(11), 3190–3196 (2019).

[21] T. Fang, T. R. Liu, Z. N. Jiang, R. Yang, P. Servati, and G. R. Xia, "Fabrication and the interlayer coupling effect of twisted stacked black phosphorus for optical applications," ACS Appl. Nano Mater. **2**(5), 3138–3145 (2019).

[22]W. Kohn and L. J. Sham, "Self-consistent equations including exchange and correlation effects," Phys. Rev. **140**, A1133–A1138 (1965).

[23]G. Kresse and J. Furthmuller, "Efficiency of *ab-initio* total energy calculations for metals and semiconductors using a plane-wave basis set," Comput. Mater. Sci. **6**, 15–50 (1996).

[24]P. E. Blochlm, "Projector augmented-wave method," Phys. Rev. B **50**, 17953–17979 (1994).

[25]G. Kresse and D. P. Joubert, "From ultrasoft pseudopotentials to the projector augmented-wave method," Phys. Rev. B **59**(3), 1758–1775 (1999).

[26]J. Heyd, and G. E. Scuseria, "Hybrid functionals based on a screened Coulomb potential," J. Chem. Phys. **118**, 8207 (2003);J. Chem. Phys. **124**, 219906 (2006).

[27]A. V. Krukau, O. A. Vydrov, A. F. Izmaylov, and G. E. Scuseria, "Influence of the exchange screening parameter on the performance of screened hybrid functionals," J. Chem. Phys. **125**(22), 224106 (2006).

[28]H. J. Monkhorst and J. D. Pack, "Special points for Brillouin-zone integrations," Phys. Rev. B **13**(12), 5188–5192 (1976).

[29]X. F. Wu, D. Vanderbilt, and D. R. Hamann, "Systematic treatment of displacements, strains, and electric fields in density-functional perturbation theory," Phys. Rev. B **72**(3), 35105 (2005).

[30]S. Ivo, J. Iniguez, and D. Vanderbilt, "First-principles approach to insulators in finite electric fields," Phys. Rev. Lett. **89**(11), 117602 (2002).

[31]F. Bloch, "Über die Quantenmechanik der Elektronen in Kristallgittern," Z. Phys. **52**, 555–600 (1929).

[32]J. C. Slater and G. F. Koster, "Simplified LCAO method for the periodic potential problem," Phys. Rev. **94**(6), 1498 (1954).

[33]J. K. Burdett and S. Lee, "The pressure-induced black phosphorus to A7 (arsenic) phase transformation: An analysis using the concept of orbital symmetry conservation," J. Solid State Chem. **44**, 415–424 (1982).

[34]Y. Takao, H. Asahina, and A. Morita, "Electronic structure of black phosphorus in tight binding approach," J. Phys. Soc. Jpn. **50**(10), 3362–3369 (1981).

[35]T. Osada, "Edge state and intrinsic hole doping in bilayer phosphorene," J. Phys. Soc. Jpn. **84**(1), 013703 (2015).

[36]P. T. T. Le, K. Mirabbaszadeh, M. Davoudiniya, and M. Yarmohammadi, "Charged impurity-tuning of midgap states in biased Bernal bilayer black phosphorus: An anisotropic electronic phase transition," Phys. Chem. Chem. Phys. **20**(38), 25044–25051 (2018).

[37]W. A. Harrison, *Electronic Structure and the Properties of Solids* (Dover, Mineola, New York, 1989).

[38]L. C. Lew Yan Voon, *Electronic Properties of Semiconductor Nanostructures* (Worcester Polytechnic Institute, 1993).

[39]E. Clementi and D. L. Raimondi, "Atomic screening constants from SCF Functions," J. Chem. Phys. **38**, 2686 (1963).

[40]N. Jörg and M. Scheffler, "Adsorbate-substrate and adsorbate-adsorbate interactions of Na and K adlayers on Al (111)," Phys. Rev. B **46**(24), 16067–16080 (1992).

[41]L. L. Li, B. Partoens, and F. M. Peeters, "Tuning the electronic properties of gated multilayer phosphorene: A self-consistent tight-binding study," Phys. Rev. B **97**(15), 155424 (2018).

[42]B. C. Deng, V. Tran, Y. J. Xie, H. Jiang, C. Li, Q. S. Guo, X. M. Wang, H. Tian, S. J. Koester, H. Wang, J. J. Cha, Q. F. Xia, L. Yang, and F. N. Xia, "Efficient electrical control of thin-film black phosphorus bandgap," Nat. Commun. **8**, 14474 (2017).

[43]Y. Q. Cai, G. Zhang, and Y.-W. Zhang, "Layer-dependent band alignment and work function of few-layer phosphorene," Sci. Rep. **4**(1), 6677 (2015).

[44]D. J. Chadi and M. L. Cohen, "Tight-binding calculations of the valence bands of diamond and zincblende crystals," Phys. Status Solidi B **68**(1), 405–419 (1975).

[45]M. Nakhaee, S. A. Ketabi, and F. M. Peeters, "Machine learning approach to constructing tight binding models for solids with application to BiTeCl," J. Appl. Phys. **128**(21), 215107 (2020).